Properties of PACE-I HgCdTe Detectors in Space - the NICMOS Warm-up Monitoring Program

T. Böker¹, J. Bacinski, L. Bergeron, D. Calzetti, M. Jones, D. Gilmore, S. Holfeltz, B. Monroe, A. Nota, M. Sosey

Space Telescope Science Institute, 3700 San Martin Drive, Baltimore, MD 21218

boeker@stsci.edu

	G. Schneider, E. O'Neil, P. Hubbard, A. Ferro, I. Barg, E. Stobie						
Steward	Observatory,	University	of Arizona, 9	33 North	Cherry Ave	enue, Tucson	, AZ 85721
	Received		;	accepted			_

¹Affiliated with the Astrophysics Division, Space Science Department, European Space Agency.

ABSTRACT

We summarize the results of a monitoring program which was executed following the cryogen exhaustion of the Near Infrared Camera and Multi-Object Spectrometer (NICMOS) onboard the Hubble Space Telescope. During the subsequent warm-up, detector parameters such as detective quantum efficiency, dark current, bias offsets, and saturation levels have been measured over the temperature range 62 K to about 100 K. The measurements provide a unique database of the characteristics of PACE-I HgCdTe detector arrays in the space environment. A surprising result of the analysis is the fact that all three NICMOS detectors showed an enhanced dark current in the temperature range between 77 K and 85 K. However, a subsequent laboratory experiment designed to replicate the onorbit warm-up did not reproduce the anomaly, despite the fact that it employed a flight-spare detector of the same pedigree. The mechanism behind the on-orbit dark current anomaly is therefore believed to be unique to the space environment. We discuss possible explanations for these unexpected observational results, as well as their implications for future NICMOS operations.

Subject headings: instrumentation:detectors

1. Introduction

The Near Infrared Camera and Multi-Object Spectrometer NICMOS (Thompson 1992; Thompson et al. 1998; Böker et al. 2000a), was installed onboard the Hubble Space Telescope (HST) during the second Servicing Mission in February 1997. NICMOS provides HST with infrared imaging and spectroscopic capabilities at wavelengths between 0.8 and $2.5 \,\mu\text{m}$. It offers three cameras with different image scales and adjacent, but not contiguous

fields. Each of the three cameras is equipped with a NICMOS-3 type, 256×256 pixel HgCdTe-detector manufactured by Rockwell.

Shortly after its on-orbit installation, it was discovered that the NICMOS dewar suffered from a thermal anomaly that led to a higher than expected sublimation rate of the solid nitrogen coolant, and thus a shortened lifetime of the instrument. After an intensified science program, operation of NICMOS for astronomical observations was suspended on Dec. 18, 1998. The cryogen was depleted on Jan. 4, 1999. Since then, the instrument has been inactive except for engineering telemetry data at the ambient temperature of the HST aft shroud ($\approx 280 \, \mathrm{K}$).

Soon after the shortened NICMOS lifetime became apparent, NASA started investigations of possible means to continue NICMOS operation. As a result of this process, the NICMOS Cooling System (NCS, Cheng et al. 1998) will be installed during the next HST servicing mission late in 2001 in order to maintain an infrared capability on HST. The NCS is a mechanical cooler which uses a closed-loop reverse-Brayton cycle to maintain the NICMOS detectors at temperatures around 75 K. The detectors when cooled by the NCS will therefore be 15-20 K warmer than during the solid nitrogen period.

In preparation for NICMOS/NCS operation, a warm-up monitoring program was initiated immediately after the NICMOS science program was completed. The main goal of this program was to utilize the one-time opportunity of the instrument warm-up to monitor the performance of the NICMOS detectors as their temperatures passed through the range expected for operations under the NCS. A good understanding of the temperature dependence of NICMOS performance is crucial for designing the instrument calibration program following its re-commissioning in order to enable optimum NICMOS science.

The NICMOS warm-up monitoring program consisted of three elements which are summarized in Table 1:

- 1. Lamp flats were taken four times a day in a number of filters in all three cameras. The goal was to follow variations of the detective quantum efficiency (DQE) as a function of temperature and wavelength. Because of safety concerns, filter wheel motions were suspended when the temperature sensors on the detector mounting cups reached 78.1 K. At this temperature, the sensor's analog-to-digital converters (ADC) reached their dynamic range limit, so that accurate temperature monitoring was no longer possible. At this point, the BLANK filter was inserted into the beam of all three cameras, and only dark current measurements were performed.
- 2. Dark current exposures were taken in all three cameras during every orbit that was not otherwise used. This program was designed to allow monitoring of both the dark current of the detectors and possible temperature-induced electronic effects, such as bias drifts. The dark current monitoring remained active until NICMOS data taking was suspended on Jan. 11, 1999 at which point the detectors had a temperature of about 115 K.
- 3. To check for possible focus variations due to changing mechanical stresses in the NICMOS dewar and fore optics, a star cluster was observed twice a week until the filter wheels were fixed in the BLANK position. This part of the program mainly addresses changes in the HST/NICMOS optics, and is not relevant to detector characterization. It is therefore not further discussed in this paper.

Except for a brief suspension of the NICMOS instrument on Dec. 24, 1998 for reasons unrelated to the warm-up, all programs executed nominally. The data, which are available from the HST archive, were analyzed in near real-time fashion, and correlated with continuous temperature readings from various sensors in the instrument. Details of the data analysis and preliminary findings are discussed in Böker et al. (1999).

In this paper, we concentrate on those results that relate to the properties of the

NICMOS-3 detector arrays. In § 2, we briefly describe the methods for monitoring the instrument warm-up temperature profile. The data format and the results of the analysis are summarized in § 3. We show the dependence of DQE, detector bias, saturation levels, and dark current as a function of temperature. While the first three items showed a behavior consistent with expectations, the dark current exhibited an unexpected increase and subsequent decline between 77 K and 85 K, which is discussed in § 4. This increase was large enough to compromise NICMOS sensitivity, if it had to be operated under these conditions. As a consequence, the NASA Independent Science Review Committee, which met in March 1999 at STScI, recommended suitable laboratory experiments to study further the cause of the anomaly, to decide whether it is likely to affect NICMOS operations under the NCS, and to investigate the possible impact on NICMOS capabilities². Following this recommendation, STScI, in collaboration with the NICMOS Instrument Definition Team at Steward Observatory, University of Arizona, designed a laboratory test program to investigate one proposed explanation for the dark current anomaly. We describe the design of the experiment as well as its hardware, setup, and results in § 5.

2. Temperature profile of the warm-up

On Jan. 4th, 1999, NICMOS telemetry data showed a sharp rise in the temperature readings of all three detector mounting cup sensors as well as all other sensors distributed across the instrument. This event marked the complete exhaustion of the solid nitrogen coolant after which the NICMOS instrument was no longer in thermal equilibrium. The exact determination of the detector temperatures as a function of time warrants some

²The final report of the committee is available online at http://www.stsci.edu/observing/nicmos_cryocooler_isr1999.html

further explanation.

All three NICMOS detectors have an on-chip temperature sensor. However, the use of these during normal NICMOS operations produces undesirable excess noise in the data. In addition, their accuracy is rather poor ($\approx 2 \, \mathrm{K}$). Therefore, we did not make use of the on-chip temperature sensors until all data taking was suspended. The overall detector temperature profile was thus derived from a combination of three data sources:

- Temperature sensors attached to the detector mounting cups for temperatures up to 78.1 K when the ADC limit was reached.
- Detector bias readings from 78.1 K until NICMOS data taking was suspended.
- The on-chip sensors after the monitoring program ended.

Figure 1 shows the temperature profile of the detectors in cameras NIC1 and NIC3. Both detectors - as well as the one in camera NIC2 which is not shown - experienced a very similar temperature profile. However, small differences exist, as is evident from the plot of the warm-up rates of NIC1 and NIC3, i.e. the gradient of the temperature profile in Figure 1. In particular, there is a delay of about 2 hours between the profiles NIC1 (and NIC2) and that of NIC3. This delay can be explained by their different locations inside the NICMOS dewar: the NIC3 detector is mounted at the front end of the dewar, further away from the N_2 ice, and therefore reacted earlier to the ice depletion than the other two cameras.

Except for this time delay, however, the rates of all sensors show a basically identical behavior: a steep increase to $\approx 7\,\mathrm{K\,day^{-1}}$ on Jan. 4 immediately following the ice depletion, a slowing of the warm-up to a rate of $\approx 5\,\mathrm{K\,day^{-1}}$ on Jan. 6, when a second rate increase to $\approx 10\,\mathrm{K\,day^{-1}}$ occurred. The most likely explanation for this second rate increase is outgassing from a charcoal getter inside the NICMOS dewar. The purpose of this getter

was to adsorb any gas that might have permeated the NICMOS vacuum seals during the pre-launch cold period. Because the adsorption capacity of a charcoal getter is a strong function of temperature (and pressure), the getter is expected to have released nitrogen and oxygen throughout the NICMOS warm-up. The gas constitutes an additional heat conduction path towards the detectors, hence the increase in the warm-up rate.

3. Results of the monitoring program

3.1. Data format

All monitoring data were obtained with the MULTIACCUM readout sequences as described in the NICMOS data handbook (Böker et al. 2000a). Briefly, the MULTIACCUM scheme is a series of non-destructive detector reads which optimize the dynamic range and allow accurate removal of cosmic rays throughout the total exposure time. In addition, variations of the pixel reset levels (or bias) can be corrected by subtracting from all further reads a frame which is taken immediately after the detector reset. This frame is called the "0th read" in the usual NICMOS terminology. The time intervals - often referred to as Δ -times - between the successive reads of a MULTIACCUM sequence can be varied. The NICMOS flight software allows a number of pre-programmed MULTIACCUM sequences. A particularly important sequence which was used extensively throughout the dark current montoring program is called STEP64. It consists of a number of reads with logarithmically increasing Δ -times up to an integration time of 64 s, and equally spaced Δ -times of 64 s beyond that.

3.2. Bias levels

Throughout the warm-up, the bias levels were monitored to prevent the signal in the high-responsivity pixels from reaching the maximum of the dynamic range of the ADCs. A procedure was put in place to quickly adjust the bias offsets, in order to prevent a significant fraction of pixels in the flat field data from reaching the ADC limit of 32,768 counts. As Figure 2 shows, the mean signal in the 0th read for all three detectors changed at a rate of $\approx 280 \,\mathrm{counts}\,\mathrm{K}^{-1}$, for a total change of about 15000 counts between 62 and 118 K. This change did not necessitate any bias adjustments during the warm-up.

Pre-launch ground testing has shown the accurate linear relationship between bias level and detector temperature to hold to at least 120 K. This justifies the use of the bias level as a thermometer to determine the detector temperature in the range where no direct readings of the mounting cup sensors are available, as described in § 2.

3.3. Amplifier glow

Amplifier glow is a well-known feature of NICMOS-3 arrays. It manifests itself as a spatially variable, but highly repeatable signal component in every detector read-out. The signal is highest in the corners of the array, i.e. closest to the read-out amplifiers, and gets fainter towards the center of the array. Typical values for the amplifier glow are 2 DN/read in the center of the array, and up to 15 DN/read in the corners. The signal is extremely repeatable and can be well modeled and removed during pipeline calibration.

The amplifier glow is measured by subtracting the first two reads in a STEP64 sequence which are only 0.3 s apart. The subtraction eliminates any contribution from the shading profile (see § 3.4), and the short integration time does not allow a significant signal from the linear dark current. The amplifier glow has been measured from the data of the dark

current program throughout the instrument warm-up. In agreement with expectations, it is constant over the entire range of our measurements.

3.4. Shading profile

The shading profile is caused by bias variations of the read-out amplifiers throughout the sequential addressing of all pixels in a detector quadrant. These bias variations have been found to be well-correlated with the time interval between readouts (Δ -time), over the full temperature range of the warm-up. The top panel of Figure 3 shows the variations of the shading profile in camera NIC2 with temperature throughout the warm-up. The median shading signal in columns 145 to 155 is plotted in the bottom panel of Figure 3 as a function of detector temperature. It can be well modeled by a second order polynomial (dash-dotted line), a fact which will be used to remove the shading during pipeline calibration (Monroe & Bergeron 1999). Since it is a noiseless contribution to the image, it can be completely removed by subtracting two reads with identical Δ -times. Subtracting the first 64 s Δ -time read from the last (after removing the accumulated amplifier glow, as described in § 3.3) therefore leaves only the signal component which is linearly accumulated during the 1000 s time interval between those two reads. This component, which is discussed in § 3.9, is usually referred to as the "true" or "linear" dark current in NICMOS data.

3.5. Detective quantum efficiency

The DQE changes as a function of temperature. The flat monitoring program was designed to determine the DQE of the NICMOS detectors at the NCS operating temperatures. Expectations were that most pixels would experience a significant increase in DQE, especially at shorter wavelengths. For the analysis, we used the data as processed

by the CALNICA pipeline ("_cal" files). To first order, this eliminates any effects caused by saturation, cosmic rays, and non-linearity. The temperature-dependent dark current and possible sky signal do not affect the analysis because each dataset consists of a pair of "lamp off" and "lamp on" exposures. Both are exposures of the (random) sky through a particular filter, but one has the additional signal from the flat field calibration lamp, which is located at the back of the Field Offset Mirror. Differencing these two exposures then leaves the true flat-field response from which the DQE increase relative to pre-warm-up can be derived. An additional complication is the fact that the pixel saturation levels also vary with temperature, as discussed in § 3.6. All pixels that showed signs of saturation during the MULTIACCUM sequence were excluded from the analysis.

For all pixels, the DQE increases roughly linearly between 63 K and 78 K, with a usually small curvature term. In all cameras, the linear slope is higher than average for the low-sensitivity regions, and lower than average for the high sensitivity regions. This behavior effectively flattens out the DQE variations across the array, as can be seen in Figure 4 which compares flat field exposures of all cameras through the F110W filter at 62 and 78 K. The histograms on the right hand side in Figure 4 clearly show a smaller spread in pixel values at the higher temperature.

Figure 5 summarizes the average DQE changes for all three NICMOS detectors as a function of both wavelength and detector temperature. The DQE increase is a well-behaved function of both wavelength and temperature. Based on the data for camera NIC3, we have linearly interpolated the measured DQE increase between the wavelengths of the employed filters for a number of temperatures. The DQE improvements are very regular and predictable. At 75 K, the expected NICMOS operating temperature under the NCS, the average responsivity increased by about 45% in J-, 33% in H-, and 17% in K-band.

Because of the regular behavior of the DQE, it is possible to create synthesized flat

fields at arbitrary temperatures and wavelengths by interpolating the model fits for each detector pixel over both parameters. These synthetic flat fields have been extensively tested, and proven to reliably reproduce the DQE for the temperature range of interest. Because the routine pipeline calibration of NICMOS data at this time cannot take into account temperature changes of the detectors, the NICMOS group provides a web-based tool to create synthetic flat field exposures for all instrument filters at arbitrary temperatures³.

3.6. Saturation levels and dynamic range

The saturation level of a given detector pixel is defined by amount of charge "loaded" onto it during the detector reset. Since the reset voltage of the NICMOS detectors is sensitive to temperature changes, the pixel saturation levels are expected to be a function of temperature. The flat field exposures taken during the course of the monitoring program allow us to measure this effect. As summarized in Figure 6 for the NIC2 camera, the average pixel saturates earlier at higher temperatures. However, the intrinsic capacitance of the detector pixels is not expected to change over the temperature range discussed here (60 K - 80 K). Therefore, the resulting loss of dynamic range at higher temperatures can be compensated by an adjustment of the reset voltage such that full use of the pixel capacitance is ensured.

³NICMOS users who wish to improve on the pipeline calibration of their data can access the tool from the NICMOS website under http://www.stsci.edu/cgi-bin/nicmos.

3.7. Readout noise

Each NICMOS detector has four independent readout amplifiers, each of which reads a 128 × 128 pixel quadrant. The noise associated with the amplification process, commonly referred to as read noise, is not expected to be a strong function of temperature. The dark current monitoring data allow us to test this expectation. Subtracting the first two reads of a STEP64 sequence eliminates all effects of bias variations or shading. The effective integration time of this difference image is only 0.3 s, too short for the linear dark current signal to become important. Therefore, the RMS deviation of the pixel values across the detector array is an accurate representation of the intrinsic read noise of the detectors. We plot the resulting read noise measurements as a function of temperature in Figure 7. From these measurements, we can confirm that the read noise is indeed fairly constant over the full temperature range covered by our data.

We converted the read noise from DN to electrons by using the following conversion gains: $5.4\,\mathrm{e^-/DN}$ for NIC1 and NIC2, and $6.5\,\mathrm{e^-/DN}$. The fact that Figure 7 shows camera NIC3 to have a slightly higher readnoise (in $\mathrm{e^-}$) than the other two cameras likely indicates that its true conversion gain is somewhat lower than assumed. In order to match the read noise levels of the other two cameras, the NIC3 gain would have to be $5.9\,\mathrm{e^-/DN}$.

3.8. Detector cosmetics

Throughout the warm-up, no evidence was found for any significant changes in the detector cosmetics, i.e. the number of hot/dead pixels remained constant, the position and amount of grot did not change, and no debonding or other mechanical pixel defects were observed.

3.9. Linear dark current

The linear dark current is measured after subtraction of amplifier glow and correction for shading. Special care was taken to minimize the impact of those measurements that were affected by high cosmic ray persistence after an HST passage through the South-Atlantic Anomaly. Figure 8 shows some example exposures that demonstrate the varying structure of the dark current throughout the warm-up. All images are shown with an identical color stretch.

The median signal of all three NICMOS arrays for the whole temperature range of the warm-up is plotted in Figure 9 on both a linear and logarithmic scale. The notable increase and subsequent decline of the dark current between 77 and 85 K is an unexpected feature to which we refer as the "bump" for the remainder of this report. An increasing number of pixels with above average dark current is responsible for the "salt and pepper" appearance of the images in Figure 8. Compared to NIC1 and NIC2, the NIC3 detector shows a much larger number of such "hot" pixels at temperatures above 85 K. This explains the elevated median dark current of NIC3 compared to the other two detectors at temperatures above 85 K (Figure 9).

3.9.1. Absence of the grot

An important observational fact is that the dark current images taken over the duration of the bump do not show any signs of "grot". Grot is the commonly used term for a number of small flecks of black paint on the detector surfaces. These particles presumably were scraped off the baffles during mechanical contact with the filter wheel housing, the process that led to the shortened NICMOS lifetime. Because grot prevents incoming photons from reaching the detector material, it is clearly visible in all NICMOS flat field images as

clusters of cold pixels, i.e. pixels with very low responsitivity. The dark current images obtained throughout the duration of the bump do not show any sign of the grot. This indicates that if NIR photons are indeed responsible for the bump, they must have come from within or behind the detector. Also, a transiently hot part inside the NICMOS dewar is inconceivable, because all temperature sensors showed a monotonic increase during the warm-up. In addition, in order to produce such a close match to flat field exposures, the signal must have been produced in or close to a pupil plane, which does not exist between the filter wheel and the detectors. One can therefore conclude that the bump signal can not be produced by NIR photons from outside the detector.

3.9.2. Morphology of the dark current bump

Another important observational result is that the morphology of the excess signal that constitutes the dark current bump closely resembles the spatial variations of the DQE. This can be most easily seen when comparing the structure in the dark current images at the peak of the bump in Figure 8 to the flat field exposures shown in Figure 4. This similarity between dark current and DQE is only seen over the temperature range of the bump signal. Any valid explanation for the dark current bump must account for this correlation, which we investigate in more detail in § 4.1.

One conclusion that can be drawn from the DQE-like bump morphology is that the electrons responsible for the bump signal are subject to the same spatial variations in material properties as "normal" signal electrons. Quantities such as impurity density, mean free path length, or recombination efficiency all affect the detection probability of a charge carrier. Therefore, the bump electrons are likely to originate at the same physical location as signal electrons produced by infrared photons.

We emphasize that a temporary rise in detector temperature can be ruled out as the source of the enhanced dark current. This is because the signal morphology at dark current levels comparable to the bump (between 90 and 96 K, Figure 8) is very different, and certainly does not reflect the DQE structure. Moreover, as described in §3.2, the detector bias levels are very sensitive to temperature changes, but certainly show no evidence for a transient heating of the detectors in excess of the overall instrument warm-up (see Fig. 2).

4. Discussion of the on-orbit dark current

The data described in the previous sections provide a comprehensive study of the performance of NICMOS-3 detectors as a function of their operating temperature. The NICMOS warm-up program offers a unique opportunity to study the effects of the space environment on HgCdTe detectors. A significant unexpected result was the elevated dark current level at temperatures between 77 and 85 K. Because the bump is located at or close to the expected operating temperature for operations under the NCS, its nature needs to be understood for successful instrument calibration. In particular, it is important to determine whether the enhanced dark current will be observed during science operation in Cycle 11 and beyond. Long exposures in narrow-band filters at wavelengths below $1.7 \,\mu m$ are of particular concern, since for these, the NICMOS sensitivity is limited by the noise associated with the dark current signal. The dark current bump observed in NICMOS therefore warrants further investigation.

The theoretical expectation for the dark current at temperatures above 140 K is to follow the charge carrier concentration (Cooper et al. 1993), which, in turn, rises with temperature according to the Boltzmann factor $e^{-E/kT}$. At temperatures between 90 and 140 K, a generation-recombination model described by Rogalski & Pietrowski (1988) provides the best agreement with the laboratory measurements of Cooper et al. (1993).

The two regimes both produce a basically linear relation of log(dark current) vs 1/T, but with different slopes. At temperatures below 90 K, poorly understood tunneling effects are known to cause a deviation from the generation-recombination model. Tunneling effects cause a flattening of the dark current curve at colder temperatures, eventually approaching an asymptotic dark current level. This behavior is also evident from Figure 9. However, none of the models predict an increase and subsequent decline in the temperature range between 77 and 85 K.

As described in § 3.9, the warm-up observations rule out both a temporary increase in detector temperature as well as a radiative signal from outside the detector as the cause for the bump. One possible origin for the charge released over the duration of the bump is a population of electrons which was "trapped" inside the detector material as long as it was colder than about 75 K. As the detectors warmed up above this threshold, the trapped charge was gradually released over the temperature range of the bump, until at about 85 K all traps were emptied. The additional charge diffuses to the pn-junctions, thus giving rise to the enhanced signal that constitutes the bump. However, this qualitative scenario leaves a number of questions open, such as the nature and number of the putative traps, the origin of the trapped charge, and the mechanism and time constants for releasing trapped charge. From the evaluation of the monitoring data, one can make a few comments that might illuminate these issues further.

4.1. The Bump-Flat Field correlation

The observed similarity of the bump morphology to the DQE variations suggests that the traps are distributed at a depth inside the bulk material of the detector roughly equal to the absorption length of infrared photons. To illustrate this point, we show in Figure 10 a cross section of the NICMOS-3 detector. Before infrared photons enter the active detector

material, they pass through a transparent sapphire substrate. In order to improve the lattice match between the sapphire and the HgCdTe material, a narrow layer of CdTe is grown between the sapphire and the HgCdTe bulk material.

Although the insertion of the CdTe layer improves the lattice match considerably, it is far from perfect, and the CdTe-HgCdTe boundary is expected to contain a large number of interface traps. If trapped electrons were indeed released at the CdTe-HgCdTe boundary, a general match between the morphologies of the bump and the DQE would be explained naturally. This is because the electrons on their diffusion path towards the pn-junction are subject to variations in the carrier lifetime inside the HgCdTe layer which give rise to non-uniformities in the DQE across the detector.

A more detailed test can be conducted by comparing the bump morphology to flat field exposures taken at various wavelengths. To first order, one would predict that flat fields taken at shorter wavelengths produce a better match to the bump structure, because shorter wavelength photons do not penetrate as deeply into the detector material as longer wavelength photons. They are absorbed closer to the CdTe-HgCdTe interface, the suggested location of the traps. If, on the other hand, the traps were distributed uniformly over the detector material, a flat field taken over the full responsivity range of the detector (i.e. $0.8 - 2.5 \,\mu\text{m}$) should provide the best match to the bump morphology.

Discriminating between these two predictions requires flat field exposures taken over a broad range of wavelengths at the temperature of the bump peak at approximately 82 K. Unfortunately, the flat field monitoring program obtained data in only a few broad-band filters (see Table 1) at only a number of temperatures below 78 K. We have therefore used the well-behaved DQE dependency on temperature and wavelength described in § 3.5, to built a set of synthetic monochromatic flat fields for a temperature of 82 K, covering the full sensitivity range of the NICMOS detectors. In Figure 11, we compare the morphology

of these to that of the bump. More specifically, we show images of the ratio between the normalized bump signal (after subtraction of the linear dark current) and the synthetic flat field exposures, sorted by wavelength. A spatially uniform ratio image means a good match between the bump signal and the DQE morphology. Obviously, the agreement is better for shorter wavelengths.

This result is quantified better in Figure 12 which plots the standard deviation in the (ring-median filtered) ratio images as a function of their wavelength. The ring-median filtering eliminates pixel-to-pixel variations and emphasizes the large-scale structures in the ratio images. For the NIC2 and NIC3 detectors, the DQE structure and the bump signal match best at the shortest wavelengths. In NIC1, the standard deviation at the shortest wavelengths is dominated by a pattern of diagonal stripes in the ratio images. These are likely due to the illumination pattern of the flat field lamps.

In summary, the fact that the best match between bump morphology and DQE is obtained at the shortest wavelengths indicates that the excess charge detected over the course of the bump originated at or close to the CdTe-HgCdTe interface. If the excess charge is indeed due to a population of traps introduced during the manufacturing process, a similar behavior would be expected in all NICMOS-3 detectors, at least in those from the same lot. The laboratory test program recommended by the Independent Science Review Committee was designed to address this question. In what follows, we describe the motivation, design, and results of this test program.

5. The "Bump Test" - A Laboratory Experiment

One proposed scenario for filling the traps is via normal signal electrons produced by infrared radiation. To test this specific hypothesis, a controlled experiment was conducted

at the NICMOS detector laboratory at Steward Observatory, University of Arizona. The goal of this program was to replicate the on-orbit warm-up profile described in § 2, and to measure the dark current of a NICMOS-3 detector as a function of temperature for two scenarios. In the first, the device was cooled down, and not exposed to any external illumination in the cold state. Since no signal electrons were produced that could fill the putative traps, the expectation is that the subsequent warm-up should not show the dark current bump. In the second scenario, the detector was flood-illuminated in the cold state, with levels exceeding the charge amount under the bump by about three orders of magnitude. In this case, one expects the putative traps to be filled before the warm-up starts, and hence the bump should be reproduced.

Details about the major elements of the laboratory equipment and the test procedures may be found in Böker et al. (2000b). Here, we only give a brief summary to illuminate some crucial aspects. The test detector - a NICMOS-3 flight spare array with characteristics that are very similar to the on-orbit detectors - was secured in a flight-like mount and installed in a dewar with a cold-shuttered optical window. The dewar contains two filter wheels which can be externally commanded and rotated for optical stimulation at selected wavelengths. A temperature-controlled stage accurately holds the array to any desired temperature. The thermal background inside the dewar produces a detector signal of about $0.3 \, \mathrm{e^-s^{-1}}$. This sets a lower limit to any dark current measurements, but is smaller than the actual detector dark current over most of the temperature range of interest.

In order to establish a baseline measurement of the dark current increase with temperature, the detector was cooled to 63.4 K without any prior illumination and allowed to thermally stabilize. After a series of dark exposures taken at this baseline temperature, the detector was warmed to 88 K through a sequence of 14 linear ramp segments. The ramp slopes were chosen to closely follow the on-orbit warm-up of the NICMOS flight

detectors, and replicated the on-orbit warm-up profile with high accuracy. During the entire duration of the warm-up (about 5 days), STEP64 MULTIACCUM exposures were taken continuously, each with a total exposure time of 1088 s. This data format is identical to that used during the on-orbit monitoring program.

Following this initial warm-up, the detector was re-cooled to 63.4 K and another set of baseline darks was obtained to provide a consistency check with the previous data. The cold detector was then exposed to a high level of incident NIR light. Four discrete passbands with a FWHM of $0.1\,\mu\mathrm{m}$ were used to cover the full range of spectral sensitivity of the array⁴. The primary goal of the flooding process was to expose the detector to broad-band illumination levels greater than the total charge released during the on-orbit bump anomaly, i.e. $\sim 8 \times 10^5\,\mathrm{e^{-pixel^{-1}}}$. However, the probability of a signal electron being "caught" in one of the putative charge traps is unknown. As a compromise between test duration and probability of filling the traps, we adopted a ~ 1000 times higher integrated flood signal. The total accumulated signal achieved over the four passbands during the flood was $1.7 \times 10^9 \mathrm{e^-/pixel}$, as detailed in Table 2. After the flood illumination, another series of baseline darks was taken. The warm-up profile and dark current measurements were then repeated identically as in the pre-flood phase. If the proposed scenario for charge traps was correct, this sequence should have reproduced the on-orbit dark-current bump.

We also investigated any systematic effects caused by the detector not being in thermal equilibrium during the warm-up. It is known, for example, that the thermal coupling between the array and its temperature sensor through the detector stage is not perfect.

This will introduce some amount of thermal lag, so that the measured dark current is

⁴In order to assure quantitative knowledge of the incident flux level, we chose not to perform the flooding unfiltered. Also, using a very broad bandpass would have saturated the detector in the shortest possible read time.

actually attributed to a slightly wrong detector temperature. To address these issues, the detector was again cooled to 63.4 K and allowed to thermally equilibriate. After another series of baseline darks, the detector was warmed through a number of thermal plateaus. At each of these (at temperatures of 63.4, 70, 77, 83, and 88 K), the detector was held stable for 5 hours. After equilibration, ten dark current exposures were obtained at each plateau. These measurements were compared to those in the same temperature regimes, during the continuous warm-up. From this comparison, we obtained an empirical measure of the heat transfer efficiency between the detector and its temperature sensor which is discussed in the next section.

5.1. Data Reduction & Analysis

For all MULTIACCUM sequences obtained throughout the test program, we measured the dark current accumulation between reads 14 and 25. The 14th read was chosen as the reference frame because it is well beyond any device non-linearities introduced by the reset gradient (a.k.a. "shading") of the device (Rieke et al. 1993). The signal difference between the two reads divided by the net integration time yields the linear dark current. We measured the three-sigma clipped mean and median dark current in each detector quadrant over a 70x70 pixel sub-array. The sub-arrays were used to avoid the bulk of the amplifier glow and other anomalies at the quadrant boundaries. The measured dark current was then related to temperature for both the pre- and post-flood test runs.

However, there is an additional complication to the interpretation of the measurements. The above measurement does not yield the true dark current, because the detector is not in thermal equilibrium. As the device warms up, the two reads - which are 704 s apart - are taken at different temperatures. This introduces a DC bias change. The DC bias, or zero point, can be measured from the 0th read in a MULTIACCUM sequence which is taken

only 0.2 s after the reset. For a detector in thermal equilibrium, the zero point depends linearly on detector temperature. In other words, NICMOS-3 detectors make excellent thermometers. For the test detector, we found a DC shift rate of $\sim 190 \,\mathrm{ADU}\,\mathrm{K}^{-1}$. The apparent signal produced by this effect was removed via the following scheme.

Based upon the thermal slew rate at any given time during the warm-up, one can easily calculate the temperature difference between reads 14 and 25 of each MULTIACCUM sequence, and hence predict the excess signal in the absence of any other effects. However, one cannot simply subtract this predicted excess signal from each dark current measurement. As mentioned before, the thermal coupling between the detector and the sensor used to control the detector temperature is imperfect. Indeed, the predicted DC drift rate underestimates the true value. The magnitude of this effect, however, can be quantified by comparing the dark current measured with the detector in thermal equilibrium at different temperatures - as done during the last phase of the test - with those measured with the detector transitioning through the same temperatures. One can then empirically find a scaling factor, which should be proportional to the thermal impedance between the detector and its temperature sensor. This scaling factor is to be applied to the predicted DC drift contribution to the measured dark current. For our instrumental set-up, the scale factor was found to be $\sim~3$, as illustrated in Figure 13. The solid gray line shows the expected signal excess at each segment of the thermal ramps after scaling. When this model of the signal excess is subtracted from the measured dark current (dots), the corrected dark current (black line) exactly passes through the measurements obtained with the device in thermal equilibrium (squares).

As can be seen from Figure 13, the measured and corrected dark current curves for the post-flood warm-up data show no evidence of any bump-like signal as seen in the on-orbit warm-up. Therefore, the proposed explanation of photoelectrons "stored" in charge traps

that are intrinsic to the manufacturing process of the NICMOS detectors seems unlikely.

6. Alternative explanations

An alternative mechanism for producing charge traps - which uniquely applies to detectors in space - is displacement damage from high-energy protons in the low-earth orbit (LEO) environment. The HST orbits the earth in an altitude of about 600 km with an orbital period of about 94 min. About half of its orbits pass through the South Atlantic Anomaly (SAA), a region where the van Allen radiation belts reach lower altitudes because of the asymmetry of the earth's magnetic field. The charged particle flux onto the HST instruments during passage through the SAA is much higher than during "SAA-free" parts of the orbit. The total on-orbit radiation dosage of the NICMOS detectors is fairly uncertain. Our best estimate is based on data from the APEXRAD software (Gussenhoven et al. 1997). Assuming a total shielding of about 10 mm of Aluminum, we derive an upper limit of $4 \,\mathrm{J\,kg^{-1}}$ over the entire NICMOS lifetime. For comparison, the average total signal integrated over the temperature range of the bump was $5.8 \cdot 10^5 \,\mathrm{e^-/pixel}$.

Another possible explanation for the bump signal, which is physically different from charge traps within the detector, is photoluminescence. Hunter et al. (1980) have shown that HgCdTe does show luminescence at energy levels within the band gap via band-to-band and donor-to-acceptor-transitions, as well as bound-exciton recombination. While the detailed mechanism remains to be identified, it is not inconceivable that luminescence - induced either by the thermal energy provided by the detector warm-up or by mechanical stress - can produce photons inside the detector material which are subsequently registered as the bump signal. Clearly, a more sophisticated test program is required to investigate this theory further.

Finally, it has been suggested that surface leakage associated with a transiently sublimed layer on the detector might be a viable explanation for the bump. In this context, the outgassing of the charcoal getter mentioned in § 2 might provide a source for the contaminant layer. None of the above scenarios can be explored further with the limited laboratory experiment described in this paper.

7. Summary

We have presented results of the NICMOS warm-up monitoring program. Detector parameters such as quantum efficiency, dark current, bias, and saturation levels have been measured over a wide temperature range. The measurements provide a unique database of the characteristics of PACE-I HgCdTe detector arrays in the space environment. The data of the NICMOS warm-up program are available from the HST archive.

We have found an unexpected increase in dark current in all three NICMOS flight detectors in the temperature range between 77 and 85 K. We have discussed qualitative scenarios for its explanation, including the possible existence of a population of charge traps within the detector material.

We have reported on a laboratory experiment undertaken to measure the dark current as a function of temperature in a detector of the same manufacture, pedigree, and operating characteristics as the flight arrays. The program was specifically designed to investigate the trapped photoelectron hypothesis. The test results did not confirm predictions of this hypothesis. The origin of the NICMOS dark current anomaly is thus likely to be unique to the space environment, the way the NICMOS detectors are operated onboard HST, or a combination of both.

We are grateful to personnel at the Rockwell Science Center and at Ball Aerospace

for their hospitality during valuable discussions on PACE-I technology and the NICMOS instrument, respectively. In particular, we would like to thank K. Vural and W. Tennant at Rockwell who helped to clarify a number of issues related to the NICMOS-3 arrays. We are indebted to W. Burmester of Ball Aerospace who not only provided his wealth of expertise on the NICMOS instrument and detectors, but also free lodging and skiing lessons for some of us. We also would like to thank M. Rieke, M. Stiavelli, and T. Casselman for helpful conversations on the possible origin of the bump.

REFERENCES

- Böker, T., Bacinski, J., Bergeron, E., Gilmore, D., Monroe, B., Sosey, M. 1999, NICMOS Instrument Science Report 99-001, Baltimore:STScI
- Böker, T., et al. 2000, "NICMOS Instrument Handbook," Version 4.0, Baltimore:STScI
- Böker, T. et al. 2000, NICMOS Instrument Science Report 00-002, Baltimore:STScI
- Cheng, E. S., Smith, R. C., Jedrich, N. M., Gibbon, J. A., Cottingham, D. A., Swift, W.
 L., & Dame, R. E. 1998, SPIE Proc., 3356, 1149
- Cooper, D. E., Bui, D. Q., Bailey, R. B., Kozlowski, L. J., & Vural, K. 1993, SPIE Proc., 1946, 170
- Gussenhoven, M. S., et al. 1997, IEEE Transactions on Nuclear Science, 44, 2161
- Hunter, A. T., Smith, D. L., & McGill, T. C. 1980, Appl. Phys. Lett., 37, 200
- Monroe, B. & Bergeron, L. E. 1999, NICMOS Instrument Science Report 99-010,
 Baltimore:STScI
- Rieke, G.H., Winters, G.S., Cadien, J, & Rasche, R. 1993, SPIE Proc., 1946, 214
- Rogalski, A. & Pietrowski, J. 1988, in "Progress in Quantum Electronics", Vol. 12, no. 2/3, 87
- Thompson, R. I., 1992, Space Science Reviews, 61, 69
- Thompson, R. I., Rieke, M., Schneider, G., Hines, D. C., & Corbin, M. R. 1998, ApJ, 492, L95

This manuscript was prepared with the AAS LATEX macros v5.0.

Table 1. Details of the NICMOS warm-up monitoring program

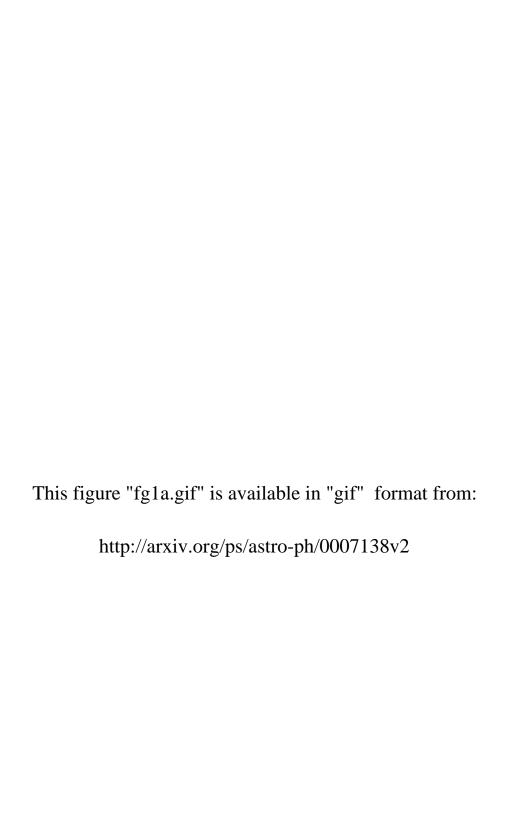
Prog. ID	Target	Purpose	Filter	
7961	random	DQE	F110W (all) F160W (all)	
			F222M (NIC3)	
7962	NGC3603	Focus	F110W (NIC2)	
			F108N (NIC3)	
7963	blank	Dark	BLANK	
(8093)				

Table 2. Flood Illumination Levels

λ_c [$\mu \mathrm{m}$]	DQE [%]	Obs. Flux $[ADU s^{-1}]$		Charge $[10^8 \mathrm{e^-pixel^{-1}}]$
0.8	0.15	3409	55	1.32
1.2	0.4	6383	78	3.51
1.8	0.6	10936	68	5.23
2.4	0.8	9189	109	7.05

- Fig. 1.— Top: temperature profile of the on-orbit warm-up of cameras NIC1 and NIC3. The curve for NIC1 has been shifted by 3 K to separate the two curves. Bottom: gradient of the temperature profile for the same two cameras. Camera 2 showed a similar behavior.
- Fig. 2.— Temperature dependence of the detector bias levels.
- Fig. 3.— Top: temperature dependence of the shading profile in camera 2. Shown are cuts along the slow readout direction for all dark exposures throughout the warm-up, with the lowest curves corresponding to the lowest temperatures. Bottom: median shading signal over columns 145 to 155 (indicated by the grey arrow) as a function of detector temperature.
- Fig. 4.— Normalized flat field exposures of all NICMOS detectors, taken through the F110W filter at temperatures of 62 K (left) and 78 K (right). The color stretch is the same for both temperatures in each camera. The histograms on the right show the flattening of the arrays at the higher temperature which can also be seen by comparing the images.
- Fig. 5.— Expected NICMOS DQE as a function of wavelength and temperature for all three NICMOS cameras. The solid lines are linear fits to the data points.
- Fig. 6.— Mean saturation level vs. temperature.
- Fig. 7.— Read noise as a function of detector temperature for all three NICMOS cameras.

- Fig. 8.— "Snapshot" dark exposures of all three cameras at temperatures of 68, 82, 88, and 96 K. Note the flat field morphology in all cameras at 82 K.
- Fig. 9.— Top: median dark current signal vs. temperature for all three NICMOS cameras. Bottom: Same, but plotted on a logarithmic scale versus 1/T.
- Fig. 10.— Cross section of a PACE-I detector array (not to scale).
- Fig. 11.— Ratio images of normalized bump signal and flat field response for various wavelengths in NIC1 (left column), NIC2 (center column), and NIC3 (right column). The color stretch is the same in all images.
- Fig. 12.— Standard deviation in the ring-median filtered ratio images of Figure 11. The filtering emphasizes the large-scale variations in the images.
- Fig. 13.— Post-flood dark currents. Dark currents measured during the warm-up thermal slews (points), with the detector held at constant temperatures (squares), and corrected (solid black line) for temperature lag (solid gray line) as discussed in the text.



This figure "fg1b.gif" is available in "gif" format from: http://arxiv.org/ps/astro-ph/0007138v2

This figure "fg2.gif" is available in "gif" format from:

This figure "fg3.gif" is available in "gif" format from:

This figure "fg4.gif" is available in "gif" format from:

This figure "fg5.gif" is available in "gif" format from:

This figure "fg6.gif" is available in "gif" format from:

This figure "fg7.gif" is available in "gif" format from:

This figure "fg8.gif" is available in "gif" format from:

This figure "fg9.gif" is available in "gif" format from:

This figure "fg10.gif" is available in "gif" format from:

This figure "fg11.gif" is available in "gif" format from:

This figure "fg12.gif" is available in "gif" format from:

This figure "fg13.gif" is available in "gif" format from: